ADVANCED MATERIALS INTERFACES
www.advmatinterfaces.de

Orientated Growth of Ultrathin Tellurium by van der Waals Epitaxy

Chunsong Zhao, Humberto Batiz, Bengisu Yasar, Wenbo Ji, Mary C. Scott, Daryl C. Chrzan,* and Ali Javey**

Tellurium, as an elemental van der Waals semiconductor, has intriguing anisotropic physical properties owing to its inherent 1D crystal structure. To exploit the anisotropic and thickness-dependent behavior, it is important to realize orientated growth of ultrathin tellurium. Here, van der Waals epitaxial growth of Te on the surface of 2D transition metal dichalcogenides is systematically investigated. Orientated growth of Te with a thickness down to 5 nm is realized on three-fold symmetric substrates (WSe_2, WS_2, $MoSe_2$, and MoS_2), where the atomic chains of Te are aligned with the armchair directions of substrates. 1D/2D moiré superlattices are observed for the Te/WSe_2 heterostructure. This method is extended to the growth of SeTe alloys, providing flexibility for band engineering. Finally, growth of textured Te film is demonstrated on the lower-symmetry surface of WTe_2.

1. Introduction

The study of the tellurium (Te) crystal structure, physical properties, and growth techniques can be traced back to the 1950s.[1] Recently, Te, as an elemental van der Waals semiconductor, is attracting resurgent interest due to its thickness and orientation dependent electronic and optical properties,[2] and application potential in electronics,[2c,3] optoelectronics,[2d] sensors,[4] modulators[5] and energy harvesting devices.[6] Te possesses a 1D crystal structure (space group $P3_121$ or $P3_221$ determined by the handedness), where atoms are arranged into spiral atomic chains via covalent bonds, and the adjacent atomic chains are packed hexagonally via van der Waals interactions[1d] (lattice parameters $a, b = 0.446$ nm, $c = 0.592$ nm). It exhibits anisotropic carrier mobility,[2b] thermal conductivity,[7] photoresponse[2d] and mechanical properties[8] stemming from the unique 1D crystal structure. To exploit the intriguing thickness and orientation dependent properties of Te, fabrication of high-quality ultrathin Te crystals with controlled orientations is critical.

Top-down exfoliation of the bulk is a common strategy to fabricate 2D materials. However, unlike some van der Waals materials such as graphite[9] and transition metal dichalcogenides (TMDs)[10] that can be mechanically exfoliated to ultrathin layers by tape, 2D formed Te has not been exfoliated from the bulk due to the relatively strong interaction between neighboring chains.[11] Liquid-phase exfoliation approaches such as sonication and electrochemical methods have demonstrated the ability to produce Te nanosheets, but the size, yield and quality of the products need to be further improved.[12] Several bottom-up approaches, such as the hydrothermal method,[2c] physical vapor deposition (PVD)[3,13] and chemical vapor deposition[14] have been explored to synthesize 2D Te. Although Te nanosheets and ultrathin films with high crystallinity and electronic properties have been achieved by these techniques, the in-plane orientation of the domains on the substrate was random in most of the work, which impedes utilization of the anisotropic properties of Te. Crystalline substrates were used to induce the alignment of the Te atomic chains.[13a,15] Te thin films and flakes grown on single crystalline MgO[13a] and mica[15b] showed a preferred orientation, where the chains are perpendicular to the substrate, so that these films are expected to have isotropic in-plane properties. Epitaxial growth of Te was observed on single crystalline KBr substrate,[15c] 2D crystals such as GaS and GaSe,[15d] and uniaxially-orientated polyethylene.[15a] Due to its inherent crystalline anisotropy, Te favors a 1D formed structure and island growth mode, leading to needle-like crystals with a large thickness (tens to hundreds of nanometers) and poor surface coverage.[13b] Therefore, oriented growth of ultrathin Te flakes and films is still challenging and lacking.

Here, we systematically investigate the van der Waals epitaxial growth[16] of Te on the surface of TMDs by PVD. Ultrathin

C. Zhao, W. Ji, A. Javey
Electrical Engineering and Computer Sciences
University of California at Berkeley
Berkeley, CA 94720, USA
E-mail: ajavey@berkeley.edu
C. Zhao, W. Ji, M. C. Scott, D. C. Chrzan, A. Javey
Materials Sciences Division
Lawrence Berkeley National Laboratory
Berkeley, CA 94720, USA
E-mail: mary.scott@berkeley.edu; dcchrzan@berkeley.edu
C. Zhao, H. Batiz, B. Yasar, W. Ji, M. C. Scott, D. C. Chrzan
Department of Materials Science and Engineering
University of California at Berkeley
Berkeley, CA 94720, USA
M. C. Scott
The Molecular Foundry
Lawrence Berkeley National Laboratory
Berkeley, CA 94720, USA
The ORCID identification number(s) for the author(s) of this article can be found under https://doi.org/10.1002/admi.202101540.

DOI: 10.1002/admi.202101540

Te crystalline films with controlled in-plane orientation have been demonstrated on several substrates with three-fold symmetric surface such as WSe_2, WS_2, $MoSe_2$, and MoS_2. The morphology of Te can be controlled from wires to flakes, or even films by tuning the growth conditions such as substrate pre-treatment and growth temperatures. The preferred growth orientation was determined by transmission electron microscopy (TEM), which showed the atomic chains were aligned along the armchair directions of these substrates. In addition, diffraction spots corresponding to the moiré structure were observed. Recently, moiré superlattice formed by stacking 2D materials shows unique physical phenomenon and properties,[17] however, there are few reports about 1D/2D moirés heterostructures. Orientated growth of SeTe alloys is also demonstrated on WSe_2, the tunable bandgap of which provides the flexibility for band alignment with other materials. The substrate system is extended from the mentioned 3-folded symmetric surfaces to lower symmetry surfaces to realize unidirectional growth of Te chains. We have achieved the growth of textured Te films on WTe_2, where all the Te grains are well aligned in all the directions and *c*-axis of Te is perpendicular to the tungsten chain direction of WTe_2.

2. Characterizations and Discussion

Ultrathin Tellurium was grown by the PVD method using a two-heating zone oven as shown in the schematic diagram (**Figure 1**a). Te powders were used as the precursor and placed in zone 1 at 450 °C. Pure Ar gas was employed as the carrier gas to deliver precursor vapor with a flow rate of 50 sccm and pressure of 1.5 Torr. TMDs flakes were exfoliated onto SiO_2/Si substrates by tape, serving as the epitaxy templates to induce the orientated growth of Te. Substrates were loaded in the downstream region (zone 2) with controlled temperatures ranging from 100 to 170 °C. Pre-annealing of the substrates and the growth temperature have critical influence on the growth (see Experimental Section). WSe_2 was used as a model TMD substrate to investigate the effect of these mentioned growth conditions.

Figure 1b,c shows the optical microscopy and scanning electron microscopy (SEM) images, respectively, of the grown Te on WSe_2 surface (WSe_2 substrate was pre-annealed at 300 °C, and substrate growth temperature was 100 °C). Unlike the 1D needle-shaped crystals in most of the published results,[13b,15a] Te grown on WSe_2 surface exhibits a 2D form with a lateral dimension of several micrometers. The nanosheets are able

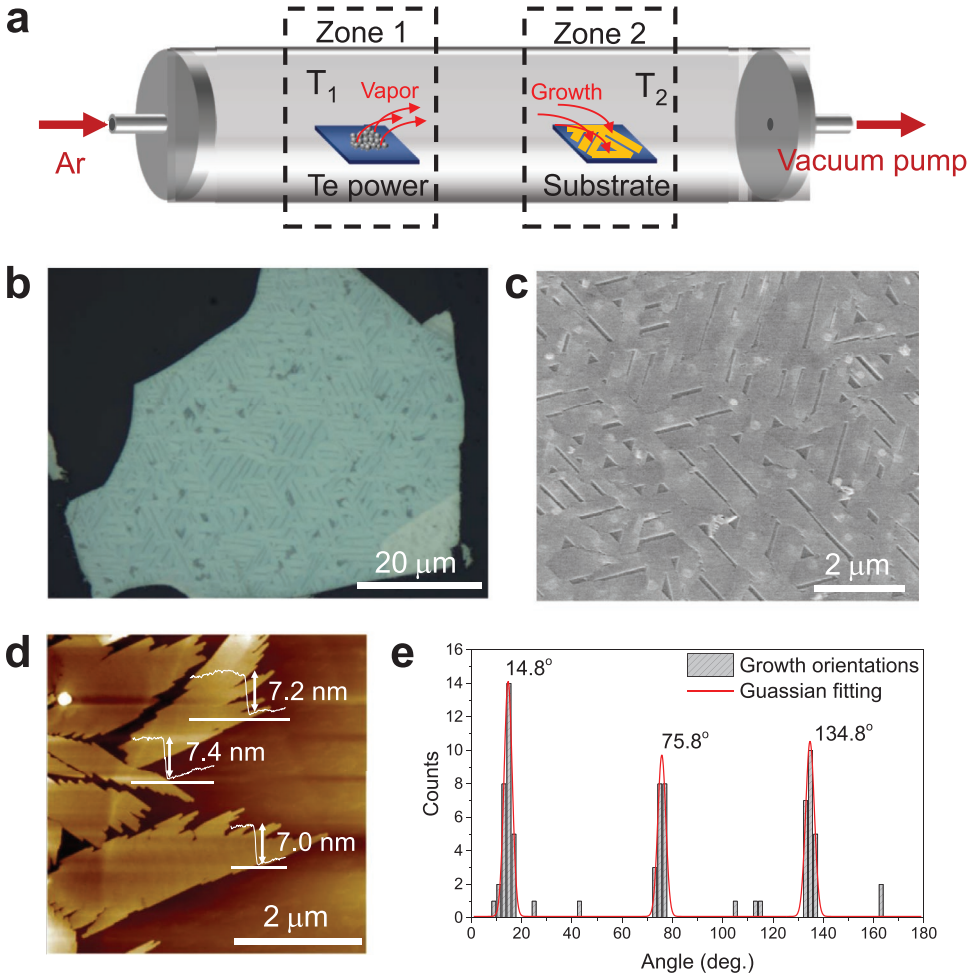

Figure 1. Characterization of Te grown on WSe_2 substrate. a) Schematic of the growth system. b,c) Optical (b) and SEM (c) images of the orientated ultrathin Te on WSe_2 substrate. d) Tapping mode AFM and the corresponding height image of the grown Te flakes. e) Statistical distribution of the orientation angle of Te in Figure S1 (Supporting Information), which is fitted by Gaussian fitting.

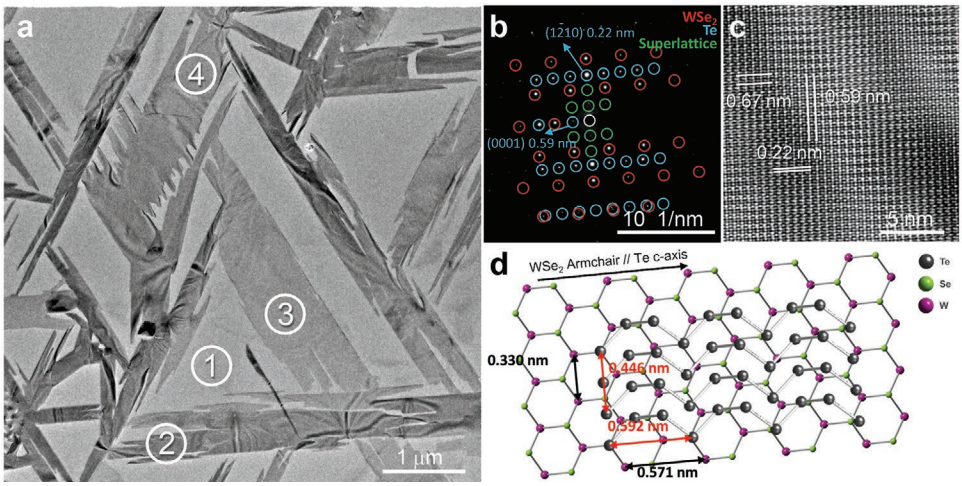

Figure 2. TEM characterization of the grown Te/WSe_2 heterostructure. a) TEM image of the Te/WSe_2 heterostructure. Electron diffraction patterns were collected from region 1 (pristine WSe_2 substrate) and regions 2–4 (Te/WSe_2 heterostructure). b,c) Selected area electron diffraction pattern (b) and Fourier-filtered HRTEM image (c) from region 2. d) Schematic of the alignment between Te atomic chains and WSe_2 surface based on b and c, where the *c*-axis of Te is parallel to the armchair direction of WSe_2.

to merge the adjacent flakes, which tend to form a continuous film. The thickness of the flakes was determined by atomic force microscopy (AFM). Te flakes have smooth surface and uniform thickness of about 7 nm as shown in Figure 1d. In addition, these flakes are well orientated on the WSe_2 surface with a peak distribution at every 60° (statistic result from 79 flakes in Figure S1, Supporting Information). Given consideration to the *C3v* symmetry of the WSe_2 surface, Te atomic chains are well aligned along the specific directions of WSe_2, indicating a van der Waals epitaxial growth.

The grown Te/WSe_2 heterostructure was transferred onto a carbon coated TEM grid. Energy dispersive x-ray spectroscopy (EDS) maps demonstrated the flakes are Te (Figure S2, Supporting Information). TEM was performed on the flakes to investigate the crystallinity of the Te nanosheets and the preferred growth orientations (**Figure 2**a). Firstly, we collected selected area electron diffraction (SAED) pattern from the WSe_2 substrate in region 1 to determine its orientation as shown in Figure S3a (Supporting Information). Then, SAED was performed on the Te flake in region 2. Two sets of diffraction patterns from Te and WSe_2 were observed in the SAED image as shown in Figure 2b, indicating the single crystalline nature of the grown Te flakes. The spots in red circles are from WSe_2 substrate, which are consistent with the data collected from region 1 (Figure S3a, Supporting Information). The Te signal has been labeled and indexed in blue. The nearest blue spots from the center correspond to the (0001) and (1-210) planes of Te, which are supported by lattice observed in the high-resolution TEM. The preferred growth direction is identified by the relative orientation between the two sets of diffraction patterns of Te and WSe_2, where the Te atomic chains are aligned along the armchair direction of WSe_2 as shown in Figure 2d. Additional weak spots, which are not from each individual layer, were observed in the diffraction pattern, and labelled in green in Figure 2b. These spots imply a periodic structure with basic translation vectors $a = 0.67$ nm and $b = 0.59$ nm. These diffraction patterns are caused by the moirés structure formed at the 1D (Te)/2D (WSe_2) van der Waals interface based on the lattice parameters of bulk WSe_2 ($a = 0.330$ nm, d-spacing 0.57 nm along armchair direction) and Te ($a = 0.445$ nm, $c = 0.592$ nm) along the [1-210] direction and *c*-axis of Te as shown in the Figure 2d. Considering a site where a Te atom is above a Se atom (or W atom, which needs further study) (Figure 2d), this site will repeat every 0.67 nm along the [1-210] direction of Te and 0.59 nm along *c*-axis of Te due to the relatively small lattice mismatch. This observed period of the superstructure might be smaller than the practical, as the Te atoms in Figure 2d are from two layers, and the inequivalence of the repeated sites is hard to distinguish due to the projective nature of conventional TEM imaging.[18] A detailed analysis on the moiré structures will be the subject of a future study. Rich physics has been discovered in the moiré structures formed by twisting and/or stacking 2D materials,[17] however, there are few reports about the construction or properties of 1D/2D van der Waals moirés superlattices. The structure grown here can be an interesting platform for the fundamental study of the 1D/2D moirés structure. We characterized two more flakes in region 3 and 4 (Figure S3c,d: Supporting Information), which showed the same preferred growth orientation and moiré diffraction patterns. These results demonstrate the orientated growth of crystalline ultrathin Te on WSe_2 by van der Waals epitaxy.

The morphology of the grown Te can be significantly influenced by the pretreatment of the substrate (see Experimental Section). As shown in **Figure 3**a, Te showed a 1D needle-like structure on the untreated, as-exfoliated WSe_2 flakes. 79% of the flakes exhibited preferred growth orientation along the armchair directions, while the other 21% flakes grew along the zigzag directions (Figure S4, Supporting Information). Te grown on the annealed substrates tends to form 2D structures as shown in Figure 3b,c. The yield of armchair orientated flakes increases to 93% after a pre-annealing of WSe_2 substrate at 200 °C (Figure 3b and Figure S4: Supporting Information). The flakes, retaining the orientated nature, grow and merge into a film with a surface coverage of 95% on the WSe_2 substrate

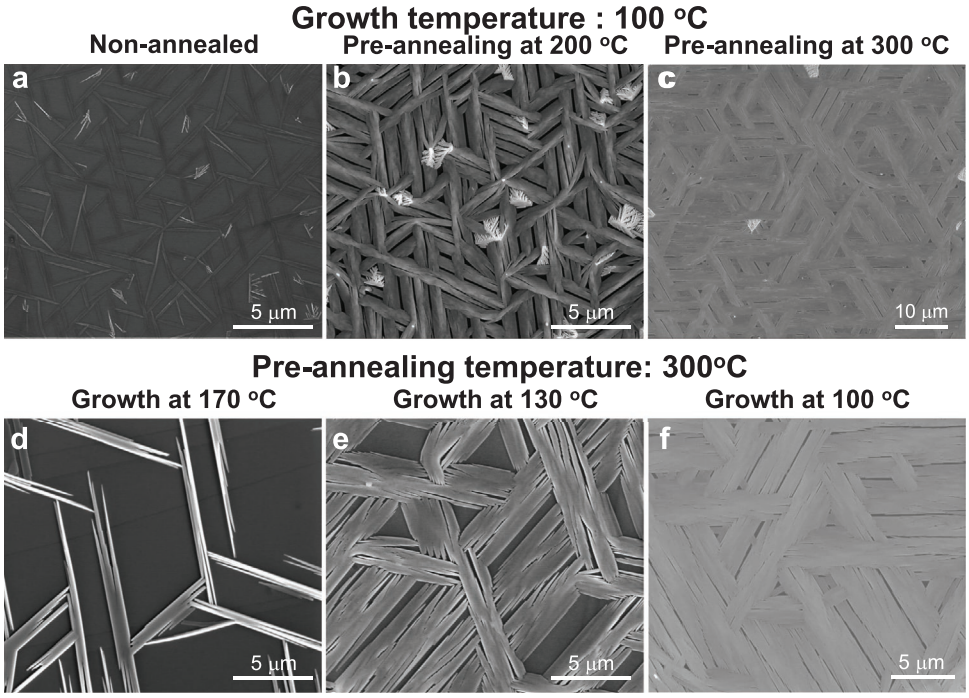

Figure 3. Morphology of Te grown on WSe_2 under different conditions. a–c) Te grown at 100 °C on the non-annealed (a), 200 °C (b) and 300 °C (c) annealed WSe_2 substrates. d–f) Te grown at temperatures of 170 °C (d), 130 °C (e) and 100 °C (f) on the 300 °C pre-annealed WSe_2 substrates.

pre-annealed at 300 °C. Figure 3a–c indicate that the films are more uniform after pre-annealing. We further investigate the influence of substrate temperature on the growth. Te was grown on the annealed WSe_2 flakes (annealing temperature was 300 °C) at temperatures ranging from 170 to 100 °C. As shown in the Figure 3d–f, the morphology of Te changes from 1D needle-like structure to 2D form with the growth temperature decreasing at fixed substrate preparation conditions.

The observed patterns of growth can be rationalized within a simple model. **Figure 4** highlights the kinetic processes that appear to be relevant to the growth mechanism. Te atoms are deposited on the surface, diffuse on that surface, and can desorb from the surface (Figure 4a–c). Note that diffusion of adatoms on a substrate with 3-fold symmetry is expected to be isotropic. The diffusing atoms can encounter trapping sites before desorption. In the case that the trapping site is another diffusing atom, a nuclei may begin to form, growing through the attachment of additional diffusing atoms (Figure 4e). Alternatively, the trapping site might be a surface defect, such as a Se vacancy in the substrate, or a Te substitutional defect in the substrate

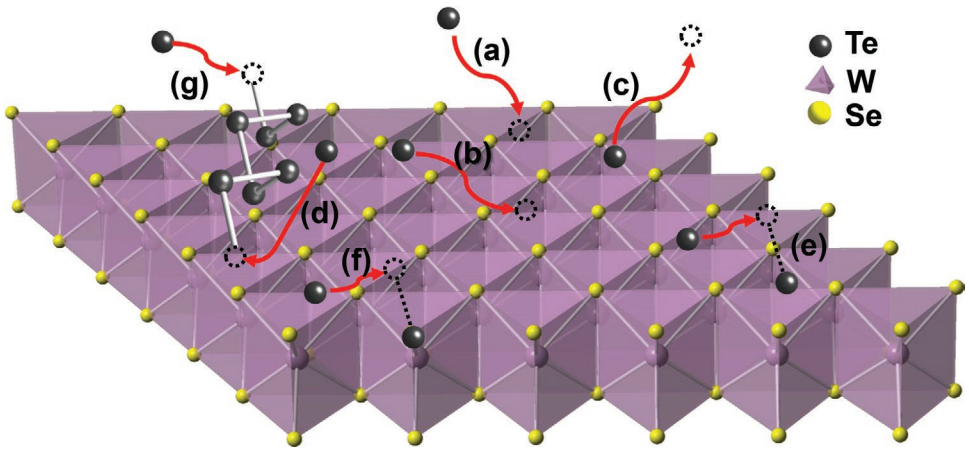

Figure 4. Kinetic Processes Affecting Morphology. a) Atoms arrive at the surface from the vapor. b) Atoms diffuse on the surface and c) may desorb from the surface, if they do not encounter a trapping site. d) Existing nuclei can serve as a trapping site. Once an atom encounters a wire, it is loosely bound and diffuses along the edge of the wire rapidly until it encounters the end of the wire, where it covalently bonds to the chain. e) Other atoms may also serve as trapping sites, leading, through standard nucleation kinetics, to homogeneous nucleation. f) Pre-existing defects can also serve as trapping sites, and can lead to heterogeneous nucleation. (Here the defect is a substitutional impurity atom.) g) After growth has progressed for some time, atoms will attach directly to nucleated clusters, and multilayer growth can ensue.

(Figure 4f). Finally, an adatom can encounter a stable cluster of Te atoms, and begin to diffuse along its edge (Figure 4d). At the first stages of nuclei growth, i.e., when the film is thin enough for the Te-substrate van der Waals interaction to be important throughout the whole nuclei, van der Waals epitaxy takes place and Te chains align with the substrate. At later stages of growth, atoms can attach directly to existing Te islands, and thus thicken the films (Figure 4g). At this later stage, the only van der Waals interaction at play is the one between the Te chains; the difference in bond strength (covalent between atoms in the same chain, van der Waals between chains) might be the mechanism behind surface roughening.

These processes can be used to understand the morphology of the growth. First and foremost, the growth shape of the crystals is determined by the relative rates of diffusion along the wire, versus diffusion at its ends. Since the Te interchain bonds are primarily of van der Waals character, one expects that edge diffusion (Figure 4d) will be very rapid relative to the diffusion of Te atoms on a pristine (0001) surface because those Te are covalently bonded to the chains. These relative rates explain the aspect ratio of the growing wires, as well as the fact that the (0001) facets of the growing plates are very rough, and perhaps even display a fingering instability.[19]

The potential for desorption helps to explain the fact that the growth rate of the films depends upon temperature and pre-annealing conditions. First, density functional theory (DFT) total energy calculations suggest that the binding energy of the Te film to the substrate is quite weak, 10 mJ m^{-2}, which is consistent with a high probability for desorption of diffusing Te atoms. (see Experimental Section for a description of the DFT calculations.) With no pre-annealing, the number of surface trapping sites (Figure 4f) is at a minimum. The potential for an atom to be bound to a trapping site is low, and the average desorption rate of the deposited Te atoms is maximized. Pre-annealing leads to the production of Se vacancies in substrate,[20] and DFT predicts that these will trap a Te atom with a binding energy of 4.9 eV. Thus, one expects that the vacancies will become substitutional Te defects. The substrate Te substitutional defects then act as a trapping site for additional Te atoms. DFT predicts that this binding energy is 1.6 eV, which is greater than that computed for a Te atom binding in a pristine substrate by 95 meV. So, on average, a Te atom has a longer residence time on the substrate for a pre-annealed sample.

The nucleation rate of clusters is probably a combination of heterogeneous and homogeneous nucleation. Consider the growth morphologies of Figure 3a–c. Clearly, pre-annealing at 200 °C leads to a higher nucleation rate than that without pre-annealing. This is most likely due to heterogeneous nucleation (Figure 4f). However, it appears that as the pre-annealing temperature is increased to 300 °C, the nucleation rate decreases. A possible explanation for this is that the vacancies produced in the substrate begin to cluster. DFT predicts that the Se divacancy in WSe_2 is bound by 105 meV. If true, as the vacancies form, the number of clusters depends on the ratio of the diffusion coefficient to the rate of production of vacancies.[21] If this ratio increases rapidly with temperature, then the number of clusters in the 300 °C pre-annealing case will be reduced relative to the 200 °C pre-annealing treatment, and the heterogeneous nucleation rate will be, accordingly, decreased.

Once the clusters are nucleated, they grow through the aggregation of atoms, both from the vapor and from the surface. Occasionally, if two atoms bound to the edge of a wire encounter one another, they can nucleate and adjacent wire, and the width of the flake increases (Figure S5a, Supporting Information). Alternatively, a Te atom diffusing along the edge of a wire may encounter and bind to a Te substitutional defect in the substrate (Figure S5b, Supporting Information). This bound atom would start a new chain that would align with the original. In this manner, the growing needles can expand to become a film.

The orientation of the wires (armchair vs zigzag) are determined by both kinetics and thermodynamics. Though the films are not strongly bound to the substrate, the symmetry of the substrate clearly impacts the growth morphology. Empirically, the chains aligned along the armchair direction seemed favored, but it is difficult to assess the relative binding energies of the two configurations using DFT because the size of the cells necessary to obtaining a low stress configuration are prohibitive.

We investigated the growth of Te on other TMDs with a similar three-fold symmetric surface structure (**Figure 5**). By employing the same method (substrate pre-annealing at 300 °C and growth at 100 °C), orientated growth of ultrathin tellurium flakes with the thickness down to 5 nm, is achieved on these 2D surfaces, indicating the possibility to build different Te based heterostructures by van der Waals epitaxy. The size of the flakes on MoS_2 and $MoSe_2$ is relatively small compared to the ones on WS_2 and WSe_2, which can be further improved by optimizing the growth conditions.

Selenium (Se) is also composed of 1D helical atomic chains, the same crystal structure as Te. It is able to be alloyed with Te to form the solid solutions for any concentration.[14b,22] These alloys have tunable bandgaps ranging from 0.3 to 1.9 eV and broad applications such as photodetectors or solar cells.[14b,22] The tunable bandgap of SeTe alloys provides flexibility for band alignment with the 2D materials, allowing the growth of functional 1D/2D heterostructures. Hence, we explored the growth of SeTe alloys on 2D surface. WSe_2 and WS_2 flakes were used as the substrates and SeTe powders with different compositions were applied as the precursor (see Experimental Section). As shown in Figure S6a (Supporting Information), orientated grown $Se_{0.3}Te_{0.7}$ crystals are achieved on the WSe_2 surface by using a $Se_{0.22}Te_{0.78}$ powders as the precursor. When the Se content of the source increases to 40% in the source, continuous $Se_{0.5}Te_{0.5}$ films are grown (Figure S6b, Supporting Information). Electron backscatter diffraction (EBSD) results show that the $Se_{0.5}Te_{0.5}$ film is polycrystalline and the misorientation between grains was ≈60° (Figure S6c–f, Supporting Information), indicating the growth mode is still van der Waals epitaxy for the alloys.

Although orientated growth of Te and SeTe crystals have been demonstrated on the above mentioned TMDs, it is hard to achieve single orientation thin films on them due to the three-fold symmetry of those TMD surfaces. However, unidirectional alignment of Te atomic chains is critical for the growth of films with properties that reflect the anisotropic nature of crystalline Te. Therefore, WTe_2 substrates, which have a relatively low-symmetry surface, were used to grow Te with a uniaxial, in-plane texture. WTe_2 has an AB stacked layered structure, where the adjacent layers are rotated 180° with respect to each other

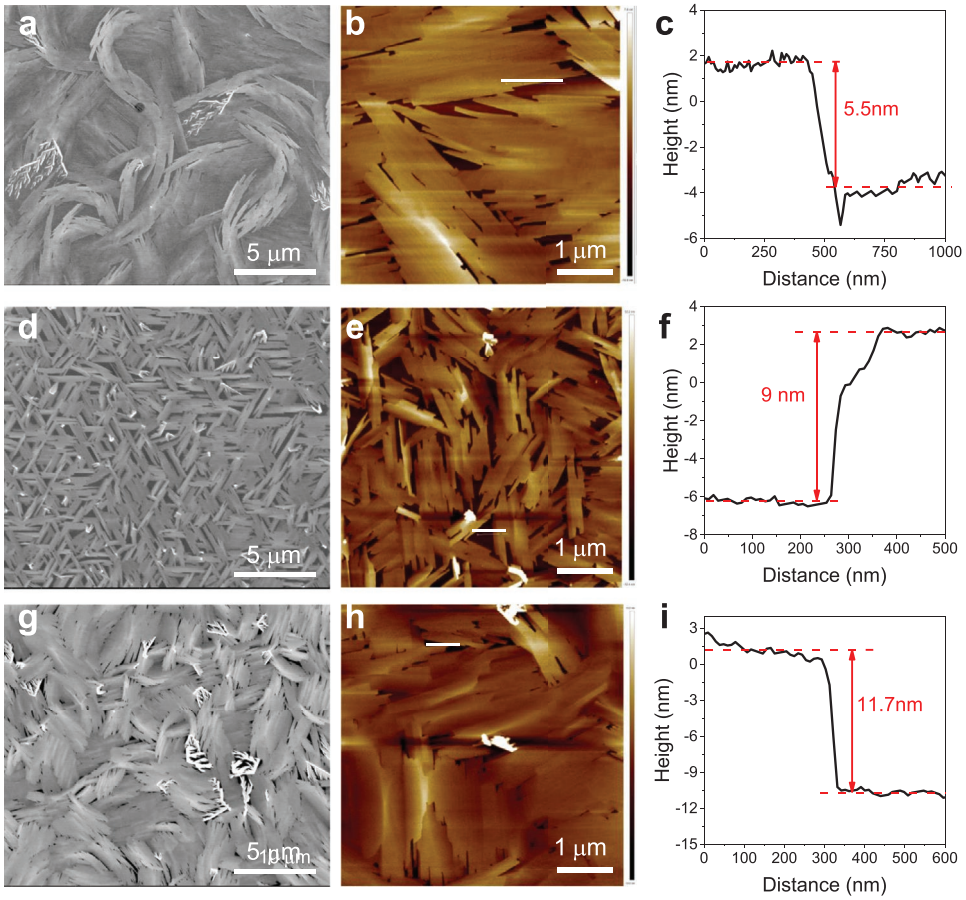

Figure 5. Orientated growth of Te on the different TMDs with three-fold symmetric surface. a–c, SEM (a), AFM (b) images and the corresponding height profile (c) of Te grown on WS_2. d–f) SEM (d), AFM (e) images and the corresponding height profile (f) of Te grown on $MoSe_2$. g–i) SEM (f), AFM (h) images and the corresponding height profile (i) of Te grown on MoS_2.

(**Figure 6**a). The surface crystal structure (*ab*-plane) has only mirror symmetry and one-fold rotational symmetry (Figure 6b) and the lattice parameters are $a = 0.350$ nm and $b = 0.628$ nm (Figure 6b), where the mismatch between *c*-aixs of Te and *b*-axis of WTe_2 is relatively small, which is in favor of the unidirectional alignment of Te atoms. WTe_2 was exfoliated onto SiO_2/Si substrates. We can determine the crystal orientation of WTe_2 flakes from their configurations, as it has the tendency to fracture along the *a*-axis during exfoliation.[23] Te was grown on the annealed WTe_2 flakes at 130 °C (pre-annealing temperature was 300 °C). As shown in the Figure 6c, we observed the growth of a continuous film with uniaxial features perpendicular to the *a*-axis of WTe_2 substrates. EBSD was performed on the Te/WTe_2 structure to determine its crystallinity and growth orientation. As shown in Figure 6d–g, the inverse pole figure (IPF) maps show constant color in all directions, indicating single-crystal-like texture of the grown Te on the WTe_2 surface. *C*-axis of Te is aligned perpendicularly to the *a*-axis of WTe_2 (tungsten atomic chains), and (10-10) planes are paralleled to the surface based on the EBSD results. Te film with (01-10) planes parallel to the surface were observed in another flake (Figure S7, Supporting Information). The different out-of-plane orientations of Te on different WTe_2 flakes is likely caused by the nature of the exposed surface of AB stacked WTe_2 substrates. Further investigation is needed for the underlying growth mechanism. Angle-resolved polarized Raman was performed on the Te and uncovered WTe_2 surface on the same flakes as shown in Figure 6h–k. The relative crystal orientation between Te and WTe_2 can be identified based on the angle-dependent intensities of the E_1-TO mode (≈94 cm^{-1}) for Te[2c] and A_1 mode (≈80 cm^{-1}) for WTe_2[23] (Figure 6j,k). The *c*-axis of Te is perpendicular to the *a*-axis of WTe_2 (Figure S8, Supporting Information), further confirming the previous results. Continuous Te thin films have been achieved by PVD methods such as thermal evaporation or sputtering. These Te films are polycrystalline and composed of random orientated micron/nano grains. In this work, although the films are still polycrystalline and the growth of individual grains results in the relatively rough surface, all the grains are aligned along the single direction and it is possible to achieve single crystalline Te films over large area by further post-annealing to eliminate the grain boundaries of the current films.

3. Conclusion

In summary, we realize orientated growth of ultrathin Te on 2D surfaces via van der Waals epitaxy. 2D Te flakes with thickness down to 5 nm are grown on the WSe_2, WS_2, $MoSe_2$, MoS_2

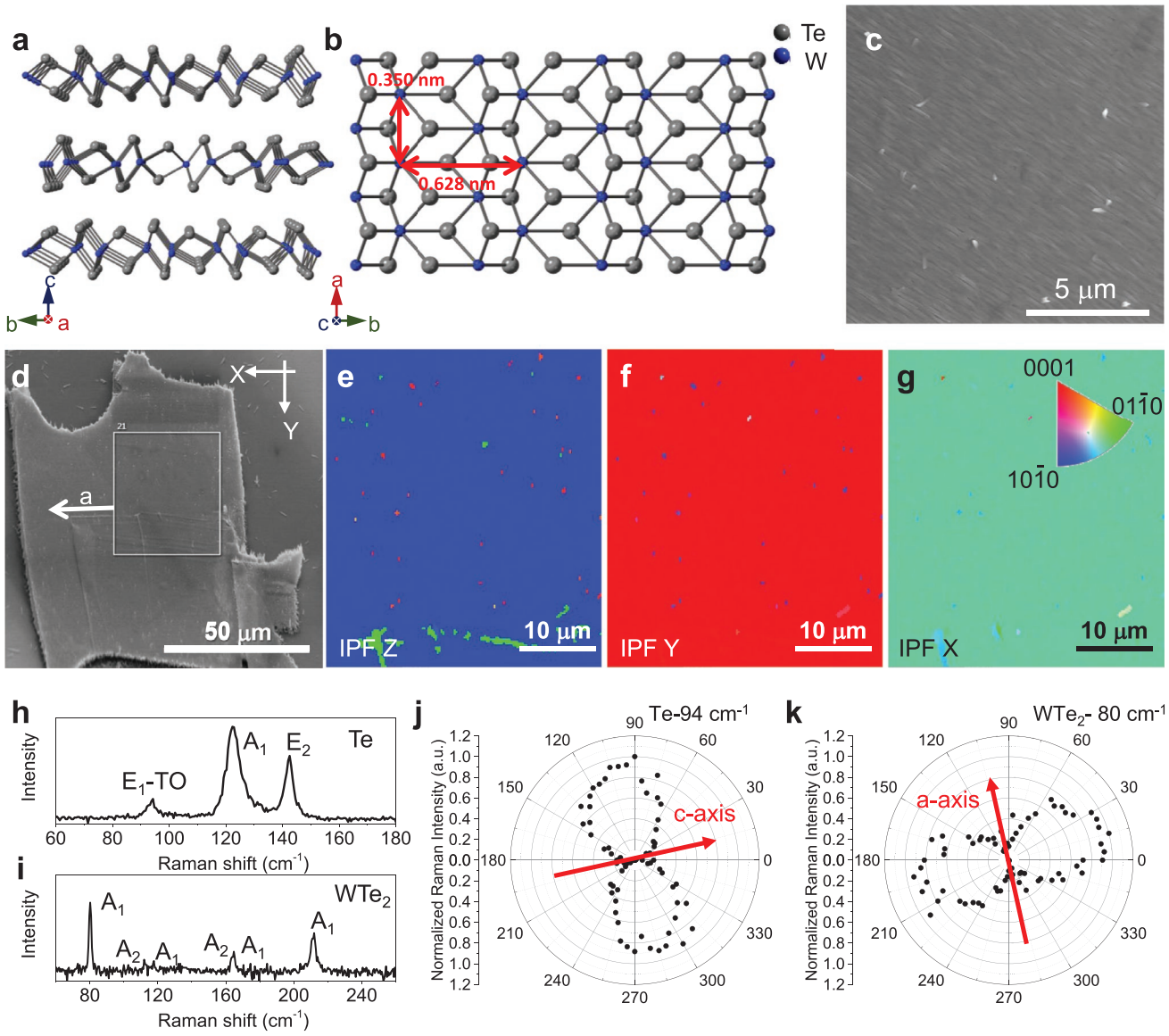

Figure 6. Unidirectional growth of Te on WTe_2 surface. a,b) Crystal structure of WTe_2 along *a*-axis (a) and *c*-axis (b). c) SEM image of Te grown on WTe_2 surface, where the uniaxial features can be observed. d–g) SEM image (d) and the corresponding EBSD IPF Z (e), Y (f), X (g) maps of Te grown on WTe_2, indicating Te atomic chains are well aligned along any directions. h,i) Raman spectrum of the grown Te (h) and the uncovered WTe_2 part (i) in the same flakes. j,k) Angle-resolved polarized Raman intensities of the peaks at 94 cm^{-1} for Te (j) and 80 cm^{-1} for WTe_2 (k). The red arrows indicate the orientations of the *c*-axis of Te and *a*-axis of WTe_2.

flakes, where the *c*-axis of Te is aligned with the armchair direction of the substrates. Moiré superlattice is achieved and observed on the Te/WSe_2 heterostructure. This method can be extended to the growth of SeTe alloys. Finally, we achieve the growth of single-crystal textured Te on WTe_2, where the *c*-axis of Te is aligned perpendicular to the tungsten chains of WTe_2.

4. Experimental Section

Materials Growth: WSe_2, WS_2, $MoSe_2$, MoS_2, and WTe_2 flakes were exfoliated onto SiO_2/Si chips as the growth substrates. The exfoliation of WTe_2 was operated in a N_2 glove box. Te pellets (99.999%, Sigma-Aldrich) or SeTe alloy crystals ($Se_{0.22}Te_{0.78}$ and $Se_{0.4}Te_{0.6}$ alloys) were grounded into powders as the precursor. Growth was done in a two-zone hot wall quartz tube furnace (Daepoong Industry, 50 602). An alumina boat containing precursor powders (20 mg) was loaded into the zone 1 of the furnace and substrates were placed in the downstream region (zone 2). Prior to the growth, the furnace was evacuated, and Ar flow was introduced at 50 sccm, at which the pressure of the system was about 1.5 Torr. Once the system is purged of air, substrates were pre-annealed at desired temperatures for 15 min. The annealing temperature was typically 300 °C. Non-annealed or 200 °C annealed substrates were used to investigate the effect of the pre-treatment in Figure 3. The furnace was open to cool down the system after pre-annealing, Ar flow and pressure were kept constant in the whole process. After pre-treatment, the substrate temperature was set to the growth temperatures (100 °C unless otherwise specified, 130 °C for the growth of Te on WTe_2). When

the substrate temperature stabilized at the target temperature, the precursor was heated to 450 °C. Ar (50 sccm) was applied as the carrier gas. The growth process last for 10–15 min. The furnace was open to cool down the system after growth.

Characterization: TEM characterization was performed on a Te/WS_2 sample. The flakes were transferred on a carbon coated transmission electron microscopy (TEM) grid by dry transfer method. TEM characterization was carried on a FEI Titan 60–300 microscope with an acceleration voltage 300 kV at the National Center for Electron Microscopy at Lawrence Berkeley National Laboratory. SEM and EBSD measurements were performed on a FEI Quanta field emission gun SEM and Oxford EBSD detector. In the analysis of the composition of SeTe alloy, SeTe was grown on WSe_2 and WS_2 flakes in the same batch, and estimated the element ratio of Se and Te by doing EDS on the alloy grown on WS_2 substrates. Performed AFM (tapping mode) was carried on a Dimension ICON AFM (Bruker, Germany).

Density Functional Theory Based Total Energy Calculations: DFT computations were run using the Vienna Ab Initio Simulation Package[19] version 5.4.4. The projected-augmented-wave method was used to model the core electrons[19b], and the exchange-correlation energy was estimated using Perdew-Burke-Ernzehof.[20] All the simulations were run using a 600 eV cutoff energy for the plane-wave (PW) basis set, a minimum spacing for the *k*-points of 0.25 $Å^{-1}$, and convergence criteria of 10^{-5} eV for the electronic self-consistent cycle (SCC). Also, a dipole correction was used in the direction perpendicular to the substrate to reduce spurious interaction with its periodic image.

To compute the binding energies of Te atoms to WSe_2 substrates with and without Se vacancies, a 5 × 5 substrate supercell was used with a 30, and the atomic positions and volume of the supercell were relaxed until the forces on all atoms were less than 10^{-3} eV $Å^{-1}$. Lastly, the binding energies were computed using the usual equation, $E_b = E_{Te/WSe_2} - (E_{WSe_2} + E_{Te})$, where E_{Te} is the energy of a single Te atom (obtained using a single *k*-point and the above mentioned parameters), and $E_{Te/WSe_2}, E_{WSe_2}$ are the energies of Te plus substrate and substrate systems, respectively.

The binding energy of a Te slab was computed using a supercell containing 1 × 4 and 1 × 3 substrate and Te unit cells, respectively, and strains of $\varepsilon_{33} = -3.6\%$ and $\varepsilon\varepsilon_{11} = -2.0\%$ were imposed on the Te slab. The bonding energy was obtained using the equation

$$E_b = \frac{E_{Te/WSe_2} - E_{WSe_2} - E_{Te}}{A} \quad (1)$$

where $E_{WSe_2}, E_{Te}, E_{Te/WSe_2}$ are the energies of the systems consisting of just the substrate, the Te slab, and the substrate plus the slab; and *A* is the area perpendicular to the substrate normal.

Supporting Information

Supporting Information is available from the Wiley Online Library or from the author.

Acknowledgements

Synthesis work was supported by the US Department of Energy, Office of Science, Office of Basic Energy Sciences, Materials Sciences and Engineering Division under contract No. DE-AC02-05CH11231 within the Electronic Materials Program (No. KC1201). Work at the Molecular Foundry was supported by the Office of Science, Office of Basic Energy Sciences, of the US Department of Energy under Contract no. DE-AC02-05CH11231. The authors thank Jun Yi for help with Raman measurements.

Conflict of Interest

The authors declare no conflict of interest.

Data Availability Statement

The data that support the findings of this study are available from the corresponding author upon reasonable request.

Keywords

moiré structure, orientated growth, tellurium

Received: August 26, 2021
Revised: October 27, 2021
Published online: January 7, 2022

[1] a) R. S. Caldwell, H. Fan, *Phys. Rev.* **1959**, *114*, 664; b) J. R. Reitz, *Phys. Rev.* **1957**, *105*, 1233; c) R. W. Dutton, R. S. Muller, *Proc. IEEE* **1971**, *59*, 1511; d) A. Koma, S. Tanaka, *Phys. Status Solidi B* **1970**, *40*, 239.

[2] a) W. Wu, G. Qiu, Y. Wang, R. Wang, P. Ye, *Chem. Soc. Rev.* **2018**, *47*, 7203; b) Z. Shi, R. Cao, K. Khan, A. K. Tareen, X. Liu, W. Liang, Y. Zhang, C. Ma, Z. Guo, X. Luo, *Nano-Micro Lett.* **2020**, *12*, 1; c) Y. Wang, G. Qiu, R. Wang, S. Huang, Q. Wang, Y. Liu, Y. Du, W. A. Goddard, M. J. Kim, X. Xu, *Nat. Electron.* **2018**, *1*, 228; d) M. Amani, C. Tan, G. Zhang, C. Zhao, J. Bullock, X. Song, H. Kim, V. R. Shrestha, Y. Gao, K. B. Crozier, *ACS Nano* **2018**, *12*, 7253.

[3] C. Zhao, C. Tan, D.-H. Lien, X. Song, M. Amani, M. Hettick, H. Y. Y. Nyein, Z. Yuan, L. Li, M. C. Scott, *Nat. Nanotechnol.* **2020**, *15*, 53.

[4] S. Sen, K. Muthe, N. Joshi, S. Gadkari, S. Gupta, M. Roy, S. Deshpande, J. Yakhmi, *Sens. Actuators, B* **2004**, *98*, 154.

[5] L. Wu, W. Huang, Y. Wang, J. Zhao, D. Ma, Y. Xiang, J. Li, J. S. Ponraj, S. C. Dhanabalan, H. Zhang, *Adv. Funct. Mater.* **2019**, *29*, 1806346.

[6] T. I. Lee, S. Lee, E. Lee, S. Sohn, Y. Lee, S. Lee, G. Moon, D. Kim, Y. S. Kim, J. M. Myoung, *Adv. Mater.* **2013**, *25*, 2920.

[7] S. Huang, M. Segovia, X. Yang, Y. R. Koh, Y. Wang, D. Y. Peide, W. Wu, A. Shakouri, X. Ruan, X. Xu, *2D Mater.* **2019**, *7*, 015008.

[8] S. Ran, T. S. Glen, B. Li, T. Zheng, I.-S. Choi, S. T. Boles, *J. Phys. Chem. C* **2019**, *123*, 22578.

[9] K. S. Novoselov, A. K. Geim, S. V. Morozov, D. Jiang, Y. Zhang, S. V. Dubonos, I. V. Grigorieva, A. A. Firsov, *Science* **2004**, *306*, 666.

[10] B. Radisavljevic, A. Radenovic, J. Brivio, V. Giacometti, A. Kis, *Nat. Nanotechnol.* **2011**, *6*, 147.

[11] a) H. O. Churchill, G. J. Salamo, S.-Q. Yu, T. Hironaka, X. Hu, J. Stacy, I. Shih, *Nanoscale Res. Lett.* **2017**, *12*, 488; b) S. Yi, Z. Zhu, X. Cai, Y. Jia, J.-H. Cho, *Inorg. Chem.* **2018**, *57*, 5083.

[12] V. Nicolosi, M. Chhowalla, M. G. Kanatzidis, M. S. Strano, J. N. Coleman, *Science* **2013**, 340, 1226419.

[13] a) E. Bianco, R. Rao, M. Snure, T. Back, N. R. Glavin, M. E. McConney, P. Ajayan, E. Ringe, *Nanoscale* **2020**, *12*, 12613; b) G. Zhou, R. Addou, Q. Wang, S. Honari, C. R. Cormier, L. Cheng, R. Yue, C. M. Smyth, A. Laturia, J. Kim, *Adv. Mater.* **2018**, *30*, 1803109; c) A. Apte, E. Bianco, A. Krishnamoorthy, S. Yazdi, R. Rao, N. Glavin, H. Kumazoe, V. Varshney, A. Roy, F. Shimojo, *2D Mater.* **2018**, *6*, 015013; d) C. Zhao, H. Batiz, B. Yasar, H. Kim,

W. Ji, M. C. Scott, D. C. Chrzan, A. Javey, *Adv. Mater.* **2021**, 33, 2100860.

[14] a) X. Zhang, J. Jiang, A. A. Suleiman, B. Jin, X. Hu, X. Zhou, T. Zhai, *Adv. Funct. Mater.* **2019**, *29*, 1906585; b) C. Tan, M. Amani, C. Zhao, M. Hettick, X. Song, D. H. Lien, H. Li, M. Yeh, V. R. Shrestha, K. B. Crozier, *Adv. Mater.* **2020**, *32*, 2001329.

[15] a) F. Katzenberg, I. Lieberwirth, J. Petermann, *J. Mater. Sci.* **1998**, *33*, 4787; b) Q. Wang, M. Safdar, K. Xu, M. Mirza, Z. Wang, J. He, *ACS Nano* **2014**, *8*, 7497; c) M. Capers, M. White, *Thin Solid Films* **1971**, *8*, 317; d) S. Yang, B. Chen, Y. Qin, Y. Zhou, L. Liu, M. Durso, H. Zhuang, Y. Shen, S. Tongay, *Phys. Rev. Mater.* **2018**, *2*, 104002.

[16] A. Koma, *Thin Solid Films* **1992**, *216*, 72.

[17] a) Y. Cao, V. Fatemi, A. Demir, S. Fang, S. L. Tomarken, J. Y. Luo, J. D. Sanchez-Yamagishi, K. Watanabe, T. Taniguchi, E. Kaxiras, *Nature* **2018**, *556*, 80; b) C. Zhang, C.-P. Chuu, X. Ren, M.-Y. Li, L.-J. Li, C. Jin, M.-Y. Chou, C.-K. Shih, *Sci. Adv.* **2017**, *3*, 1601459.

[18] K. Reidy, G. Varnavides, J. D. Thomsen, A. Kumar, T. Pham, A. M. Blackburn, P. Anikeeva, P. Narang, J. M. LeBeau, F. M. Ross, *Nat. Commun.* **2021**, *12*, 1290.

[19] G. Bales, A. Zangwill, *Phys. Rev. B* **1990**, *41*, 5500.

[20] a) M. Donarelli, F. Bisti, F. Perrozzi, L. Ottaviano, *Chem. Phys. Lett.* **2013**, *588*, 198; b) S. Tongay, J. Suh, C. Ataca, W. Fan, A. Luce, J. S. Kang, J. Liu, C. Ko, R. Raghunathanan, J. Zhou, *Sci. Rep.* **2013**, *3*, 2657; c) W. H. Blades, N. J. Frady, P. M. Litwin, S. J. McDonnell, P. Reinke, *J. Phys. Chem. C* **2020**, *124*, 15337; d) Y. Sun, X. Zhang, B. Mao, M. Cao, *Chem. Commun.* **2016**, *52*, 14266.

[21] G. Bales, D. Chrzan, *Phys. Rev. B* **1994**, *50*, 6057.

[22] I. Hadar, X. Hu, Z.-Z. Luo, V. P. Dravid, M. G. Kanatzidis, *ACS Energy Lett.* **2019**, *4*, 2137.

[23] Q. Song, X. Pan, H. Wang, K. Zhang, Q. Tan, P. Li, Y. Wan, Y. Wang, X. Xu, M. Lin, *Sci. Rep.* **2016**, *6*, 29254.